Cumulus Convection in Shear Flow—Three-Dimensional Numerical Experiments

WILLIAM R. COTTON AND GREGORY J. TRIPOLI

Department of Atmospheric Science, Colorado State University, Fort Collins 80523

(Manuscript received 14 November 1977, in final form 21 April 1978)

ABSTRACT

A three-dimensional model of deep, moist convection is described. The model is fully compressible and utilizes a "time-splitting" method of integration in order to make the model economically feasible.

This study represents an extension of the numerical experiments reported by Cotton (1975). In that work the profiles of the ratio of average cloud water content to the moist-adiabatic water content ($\bar{Q}_c/Q_A$) predicted by a one-dimensional Lagrangian (1DL) and a one-dimensional time-dependent (1DTD) model are compared with case study observed data and the average $\bar{Q}_c/Q_A$ profiles reported by Warner (1970a). In this work, data predicted by a three-dimensional (3D) cloud simulation in a stagnant environment and a 3D cloud simulation in the observed shear flow are compared with observed data and the earlier model calculations. The results of this study demonstrated that all the cloud simulations in an initially stagnant environment, including the 1DL, 1DTD and 3D models, predicted profiles of $\bar{Q}_c/Q_A$ which exhibited very high magnitudes near the top of the rising cloud. The predicted magnitudes of $\bar{Q}_c/Q_A$ near the top of the rising cloud exceeded the observed magnitude by as much as a factor of 3. In contrast, the 3D simulation in the observed shear flow predicted profiles of $\bar{Q}_c/Q_A$ and magnitudes of peak $\bar{Q}_c/Q_A$ which were in good agreement with observations.

What is most surprising is that the improved prediction of cloud liquid water content was not at the expense of the prediction of cloud-top height. Instead the cloud-top heights predicted in both the no-motion and shear-flow simulations were identical and equal to the observed cloud-top height. This is in contrast to the earlier 1DL and 1DTD model numerical experiments reported by Cotton using the same sounding. In those calculations, predicted cloud-top height varied considerably (over several kilometers) with different entrainment rates and eddy exchange coefficients. As a further benefit, the prediction of cloud-scale averaged vertical velocity in the shear-flow simulation was also better than that predicted in the no-motion simulation.

It is thus concluded that the interaction of a cumulus cloud with an environment characterized by vertical shear of the horizontal wind is a major control on the prediction of cloud internal properties. Associated with the improved prediction of $\bar{Q}_c/Q_A$, the 3D simulation in shear flow also exhibited major changes in the structure of the cloud circulation. A particularly interesting feature was the formation of rotating cloud elements in several portions of the main cloud element.

1. Introduction

Several years ago Warner (1970a) concluded that simple one-dimensional entrainment models such as those developed by Weinstein and Davis (1968), Simpson and Wiggert (1971) and Cotton (1972b) could not simultaneously predict the observed cloud top height and the observed liquid water contents of cumulus clouds. Warner arrived at his conclusion by comparing entrainment model predictions of the ratio of cloud liquid water content $\bar{Q}_c$ to the moist adiabatic value Q_A for specific cases against the observed profile of $\bar{Q}_c/Q_A$ averaged over a large sample of cloud observations. In each test case the cloud model was initiated as a saturated parcel at the observed cloud base and the entrainment coefficient was adjusted until the model predicted the observed cloud-top height. He found that the entrainment model consistently overpredicted the observed magnitude of $\bar{Q}_c/Q_A$ at levels above cloud base. Such a conclusion represents a severe criticism of one-dimensional entrainment models because a proper prediction of liquid water content is essential to the prediction of rainfall, the estimation of weather modification potential, and the parameterization of the effects of cumulus clouds on larger scale meteorological systems.

Subsequent to this study, Cotton (1975) compared the profile of $\bar{Q}_c/Q_A$ predicted with a one-dimensional entrainment model (1DL) against the observed profile of $\bar{Q}_c/Q_A$ for a specific case study rather than that obtained from the average of a large body of cloud observations. It was pointed out that the simulation of a case study may shed further light on the physics of the problem by eliminating uncertainties in the data due to cloud-to-cloud variability and the unsteady nature of convection. For example, Simpson (1971) claimed that Warner's apparent negative results were a

0022-4928/78/1503-1521$09.50

consequence of his neglect of the fallout of precipitation from the towers. While it is difficult to assess the contribution of precipitation to the dynamics of the cumuli composing Warner's large body of data, it is relatively easy to examine cloud droplet samples, aircraft observer notes and ground observer notes obtained on an individual case to determine if the cloud contained sufficient precipitation to affect the cloud dynamics. Cotton examined the records of the selected case-study day and after flying with Warner and evaluating his observer expertise, concluded that the observed cloud contained little, if any, precipitation. Cotton then found that the entrainment model again predicted values of $\bar{Q}_c/Q_A$ which were consistently greater than those observed for the case study. The one exception was for a simulation under the rather arbitrary model assumption that the predicted cloud-top height was equal to the predicted height of the parcel of air (or cloud center of mass) plus the cloud radius. For this case, the model predictions agreed with the uppermost observed $\bar{Q}_c/Q_A$ but exceeded the observed value at all other levels.

In a second part of the same investigation, Cotton (1975) compared the profiles of $\bar{Q}_c/Q_A$ predicted with a one-dimensional time-dependent model closed with an eddy viscosity parameterization of the Smagorinsky type with the case study observed $\bar{Q}_c/Q_A$ profiles. In this study Cotton also initiated the model with a moist, saturated bubble and adjusted the mixing length coefficient until the model predicted the observed cloud-top height. The predicted profiles of $\bar{Q}_c/Q_A$ exhibited a characteristic pattern of large values of $\bar{Q}_c/Q_A$ near the top of the simulated cloud with smaller values below. The profiles were not significantly altered by using the pure deformation model of eddy viscosity or by employing the buoyancy enhanced form suggested by Lilly (1962). Because the predicted magnitude of $\bar{Q}_c/Q_A$ at any given level decreased with time, it was suggested that part of the discrepancy between the high initial values of predicted $\bar{Q}_c/Q_A$ and the observed values may be attributed to the penetration of the aircraft into the cloud during a slowly decaying state. Apparently because of the unrealistic initialization of the model with a bubble, however, the simulated cloud base rapidly rose with time and the cloud decayed much faster than the observed cloud. Cotton concluded that, had a more persistent cloud-base flux been imposed or simulated, the predicted magnitude of $\bar{Q}_c/Q_A$ at any level would have remained closer to the initially high values. Thus, it appears that neither the one-dimensional entrainment model nor the time-dependent model can simultaneously predict cloud-top height and the observed profile of $\bar{Q}_c/Q_A$. Cotton then concluded that this consistent pattern of overprediction of cloud properties suggests that a larger fraction of the cloud scalar fluxes, kinetic energy and buoyancy may be on the fluctuating field as opposed to the cloud-scale averaged field.

The purpose of this paper is to further explore the factors contributing to cloud-height and liquid water content by performing fully three-dimensional simulations of cloud growth in a shearing and a no-motion environment. The results of these numerical experiments will be compared and contrasted with the previously described one-dimensional calculations as well as a two-dimensional rectilinear cloud simulation. All the model simulated data will also be compared and contrasted with the available observational data reported by Cotton (1975).

It must be recognized at the onset, however, that while the data obtained by Warner in the selected case is of high quality, it is far too sparse to provide an adequate basis for verifying the predictions of a three-dimensional model. Such factors as lack of definition of surface heating and/or orography, and a description of the mesoscale organization and forcing of the cloud systems introduce major uncertainties in specifying the cloud initiation processes. In addition, the aircraft observed data provide little or no time resolution of the cloud behavior. Thus, the main value in comparing the 3D model predicted data with the observed data is to lend a degree of credibility to the model predictions and to use the model predicted data to assist in interpreting such sparce observations.

2. Description of the three-dimensional cloud model

a. *The average equations*

The current 3D cumulus model is built upon a fully elastic set of generalized Boussinesq equations integrated in the (x,y,z) coordinate system. The dependent variables are the three velocity components, pressure perturbation, potential temperature, water vapor and cloud water. All scalar dependent variables are decomposed into three levels in the form

$$P(x,y,z,t)=P_0(z)+\bar{P}'(x,y,z,t)+P''(x,y,z,t)$$
$$=\bar{P}(x,y,z,t)+P''(x,y,z,t),$$

where P_0 is the large scale average, $\bar{P}'$ the nonturbulent fluctuation about P_0 and P'' the turbulent fluctuation about the local average. We will henceforth replace $\bar{P}'$ with p' in our notation. The velocity components are decomposed such that

$$u_i=\bar{u}_i+u_i'',$$

which is similar to the scalar variables, except that a reference state velocity u_{i_0} is not referred to. In the present model, the equations are averaged over the grid truncation scale.

The resulting averaged equations are as follows.

1) EQUATIONS OF MOTION

$$\frac{\partial \bar{U}_i}{\partial t}+\frac{1}{\rho_0}\frac{\partial P'}{\partial x_i}=-\frac{\partial \bar{U}_i\bar{U}_j}{\partial x_j}+\bar{U}_i\frac{\partial \bar{U}_j}{\partial x_j}+\epsilon_{ijk}f_j\bar{U}_k$$
$$+\delta_{i3}g\left(\frac{\theta_v'}{\theta_{v_0}}-\frac{1}{\gamma}\frac{P'}{P_0}+\bar{Q}_c\right)-\frac{\partial}{\partial x_j}(\overline{U_i''U_j''})=RU_i, \quad (1)$$

where it has been assumed that the turbulent fluctuating field is incompressible. Note that the pressure gradient term, which contributes to propagation of high-phase-speed acoustic waves has been separated from the other terms. The lower frequency terms are represented by RU_i and are the terms on the right-hand side (RHS) of (1). The divergence term on the RHS of (1) arises from the transformation of the advective term $[-U_i(\partial U_j/\partial x_i)]$ into the quadratic form $[-\partial(\bar{U}_i\bar{U}_j/\partial x_j+\bar{U}_i(\partial \bar{U}_j/\partial x_j)]$. This was done in order to make the model quasi-conservative in the mean quadratic properties as represented on a finite-difference mesh. Since the time-scale associated with advection is considerably longer than that of acoustic waves, the resulting divergence term is treated as an acoustically inactive term. The buoyancy term on the RHS of (1) largely responds to frequencies greater than the Brunt–Väisälä frequency and is therefore treated as an acoustically-inactive term. The remaining terms on the RHS of (1) (the third and fifth terms) are associated with the Coriolis and advection time scales, respectively, which are considerably longer than the acoustic time scales.

2) PRESSURE TENDENCY EQUATION

The pressure tendency equation for a compressible system is

$$\frac{\partial P'}{\partial t}-\gamma P_0\frac{\partial \bar{U}_j}{\partial x_j}=-\frac{\partial P'\bar{U}_j}{\partial x_j}+P'\frac{\partial \bar{U}_j}{\partial x_j}$$
$$+\delta_{j3}\rho_0 g\bar{U}_j+\frac{\gamma P_0}{\theta_{v_0}}\frac{d\bar{\theta}_v}{dt}-\frac{\partial}{\partial x_j}(\overline{U_j''P''})$$
$$=\mathrm{RP}. \quad (2)$$

The acoustically active portions of (2) are again given by the left-hand side (LHS) and the acoustically inactive by the RHS, i.e., RP. The first, second, third and fifth terms on the RHS of (2) are also associated with the time-scale of advective processes and are, therefore, considered acoustically inactive. The fourth term on the RHS represents the contribution to the pressure tendency by water phase changes including saturated ascent [Eqs. (6) and (7)] and isobaric mixing [Eq. (11)]. This term is likewise acoustically inactive by virtue of the fact that the hydrostatic approximation has been used to estimate the pressure contribution to (6) thus decoupling the moist thermodynamics from the acoustic modes.

3) THERMODYNAMIC ENERGY EQUATION

The thermodynamic energy equation for a moist atmosphere is

$$\frac{\partial \bar{\theta}}{\partial t}=-\frac{\partial \bar{\theta}\bar{U}_j}{\partial x_j}+\bar{\theta}\frac{\partial \bar{U}_j}{\partial x_j}+\delta_m\frac{d\bar{\theta}}{dt}\Big)_{\text{moist}}-\frac{\partial}{\partial x_j}(\overline{\theta''U_j''}), \quad (3)$$

where

$$\delta_m=\begin{cases}1, & \text{saturated}\\ 0, & \text{unsaturated.}\end{cases}$$

4) CONTINUITY EQUATIONS FOR WATER VAPOR (q_v) AND CLOUD WATER (Q_c) MIXING RATIOS

Comparable equations for moisture conservation and liquid water conservation are

$$\frac{\partial \bar{q}_v}{\partial t}=-\frac{\partial \bar{q}_v\bar{U}_j}{\partial x_j}+\bar{q}_v\frac{\partial \bar{U}_j}{\partial x_j}+\delta_m\frac{d\bar{q}_s}{dt}\Big)_{\text{moist}}-\frac{\partial}{\partial x_j}(\overline{q_v''U_j''}), \quad (4)$$

$$\frac{\partial \bar{Q}_c}{\partial t}=-\frac{\partial \bar{Q}_c\bar{U}_j}{\partial x_j}+\bar{Q}_c\frac{\partial \bar{U}_j}{\partial x_j}-\delta_m\frac{d\bar{q}_s}{dt}\Big)_{\text{moist}}-\frac{\partial}{\partial x_j}(\overline{Q_c''U_j''}). \quad (5)$$

The saturation vapor mixing ratio $\bar{q}_s$ is evaluated by using a Taylor's series approximation to Poisson's equation to obtain temperature and a Taylor's series approximation of the Goff–Gratch equation for saturation vapor pressure as described by Derickson and Cotton (1977). While the model contains a precipitation parameterization described by Cotton (1972a) and Cotton (1975), the experiments to be described below represent nonprecipitating clouds.

5) LATENT HEATING BY CONDENSATION

If a grid point is saturated, latent heat is released during vertical ascent, changing θ at the rate

$$\frac{d\bar{\theta}}{dt}\Big)_{\text{moist}}=\frac{\dfrac{\bar{W}\bar{\theta}\bar{q}_s}{\bar{T}_v\bar{T}}\left(\dfrac{\epsilon L_{vl}}{c_p\bar{T}}-1\right)\dfrac{gL_{vl}}{Rc_p}}{\dfrac{\epsilon L_{vl}^2\bar{q}_s}{Rc_p\bar{T}^2}+1} \quad (6)$$

and q_v at the rate

$$\frac{dq_s}{dt}\Big)_{\text{moist}}=-\frac{c_p\bar{T}}{L_{vl}\theta}\frac{d\theta}{dt}\Big)_{\text{moist}}. \quad (7)$$

6) SATURATION ADJUSTMENT

After each iteration in the water conservation equations, each grid point is isobarically adjusted as

follows:

$$\Delta Q_c)_{SA} = -\min\left[\frac{\bar{q}_v - \bar{q}_s}{1+\frac{\epsilon \bar{q}_s L_{vl}^2/R}{(c_p+c_v\bar{q}_v+c_w\bar{Q}_c)\bar{T}^2}}, \bar{Q}_c\right], \quad (8)$$

$$\Delta q_v)_{SA} = -\Delta Q_c)_{SA}, \quad (9)$$

$$\Delta\theta)_{SA} = \frac{-\bar{\theta}L_{vl}\Delta q_v)_{SA}}{T_0(c_p+c_v\bar{q}_v+\bar{Q}_c c_w)}. \quad (10)$$

The contribution to the pressure tendency by isobaric mixing is given by

$$\left(\frac{\partial p'}{\partial t}\right)_{SA} = \frac{\gamma P_0}{\theta_{v_0}}\left(\frac{\Delta\theta)_{SA}(1+0.61\bar{q}_v)+(\bar{\theta})(0.61)\Delta q_v)_{SA}}{2\Delta t_L}\right). \quad (11)$$

b. Turbulence closure

Eqs. (1)–(5) are closed using a first-order turbulent transport model. The form of stress used is similar to the buoyancy enhancement model presented by Lilly (1962) and discussed by Cotton (1975), in which the stress is proportional to the deformation of the mean field. The formulation is

$$-\overline{U_i'' U_j''} = K_m\left(\frac{\partial \bar{U}_i}{\partial x_j}+\frac{\partial \bar{U}_j}{\partial x_i}\right), \quad (12)$$

where K_m is an eddy exchange coefficient for momentum. The contraction term employed by Deardorff (1970) is ignored in (12) because it makes a very small contribution to the overall solution and furthermore requires an additional approximation to a model of questionable applicability to this problem. The corresponding model for scalar properties is

$$-\overline{U_i'' A''} = K_H\frac{\partial \bar{A}}{\partial x_i}, \quad (13)$$

where the K_H is the eddy exchange coefficient for heat, assumed to be the same for all scalar variables. The exchange coefficients are determined by

$$K_m = \max\left[(0.16\sqrt[3]{(\Delta x)(\Delta y)(\Delta z)})^2 0.7071 D_{ij} \times\left(1-\frac{K_H}{K_m}\mathrm{Ri}\right), (0.2\times 10^4\ \mathrm{m^2\ s^{-1}})\right], \quad (14)$$

$$K_H = \max\left[K_m\frac{K_H}{K_m}, (0.2\times 10^4\ \mathrm{m^2\ s^{-1}})\right], \quad (15)$$

where

$$K_H/K_m = 3, \quad (16)$$

$$\mathrm{Ri} = \left(\frac{g}{\bar{\theta}_v-\bar{Q}_c\theta_{v0}}\right)\left[\frac{\partial(\bar{\theta}_v-\bar{Q}_c\theta_{v0})}{\partial Z}-\frac{\partial\bar{\theta}_e}{\partial Z}\right]\Big/ D_{ij}^2, \quad (17)$$

where $\bar{\theta}_e$ is the equivalent potential temperature.

The deformation tensor is given by

$$D_{ij} = \left[\sum_j\sum_i\left(\frac{\partial U_i}{\partial x_j}+\frac{\partial U_j}{\partial x_i}\right)^2\right]^{\frac{1}{2}}. \quad (18)$$

The coefficient 0.16 in (14) was deduced from the numerical experiments reported by Cotton (1975). This closure is being used temporarily, while a more comprehensive second-order closure developed by Manton and Cotton (1977) is being tested.

c. Finite differencing

A space-staggered grid is used where all velocity variables are offset as follows:

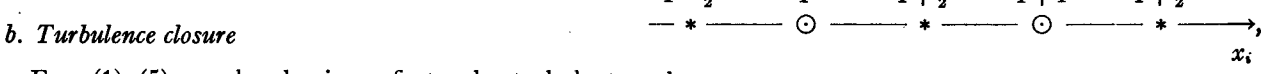

where

$$*\equiv \bar{U}_i, \quad \odot \equiv \bar{P}, \bar{\theta}, \bar{q}_v, \bar{Q}_c.$$

The subscripts I, $I+1$, ... represent the center of the grid box and $I-\frac{1}{2}$, $I+\frac{1}{2}$, $I+\frac{3}{2}$... represent subscripts of the grid box boundaries.

Standard second-order finite differencing is used on the staggered mesh providing an operator which is conservative in quadratic properties. The grid resolution selected for this study is $\Delta z = 100$ m and Δx, $\Delta y = 200$ m expanding to Δx, $\Delta y = 700$ m and $\Delta z = 250$ m near the lateral and upper boundaries, respectively. The actual grid point locations can be seen by the tick marks along the axis in the illustrated vertical and horizontal cross sections of simulated data.

Since this is an acoustic model, extremely small time steps are required. In order to make such a model economically feasible, a "time-splitting" method of integration suggested by J. Klemp (personal communication) was employed in conjunction with a leapfrog time-differencing scheme. Recently Klemp and Wilhelmson (1978) have described a similar form of the "time-splitting" method of integrating a compressible system.

The idea behind this procedure is to divide variable time tendencies into terms which are acoustically active and those which are not. This division has already been demonstrated for Eqs. (1) and (2). Tendency Eqs. (3)–(5) contain no acoustic terms. With this division made, the model is then integrated simultaneously on two levels having two timesteps of some integer ratio to each other such that acoustic terms are calculated on a much smaller timestep than the nonacoustic terms. Assuming the most expensive calculations lie in the nonacoustic terms, the model becomes much more efficient. In fact, it was pointed out by Klemp that, in his own test experiments, this procedure is economically competitive with an anelastic model in which pressure is diagnosed from the inversion of a three-dimensional Helmholtz equation. The beauty

of this scheme is that, with no significant loss in efficiency, one gains the ability to model elastic processes, and one is less dependent on lateral boundary conditions and coordinate stretching than one is with an anelastic system. Furthermore, in contrast to the inversion of a three-dimensional elliptic equation, the acoustic calculation is an easily vectorizable code thus enabling even greater gains in efficiency on such vector-based computers as the NCAR/CRAY I computer.

The exact procedure is as follows:

We consider only Eqs. (1) and (2), as Eqs. (3)–(5) are integrated in a normal leapfrog fashion with the long time step. We may rewrite Eqs. (1) and (2) as

$$\frac{\partial \bar{U}_i}{\partial t} = -\frac{1}{\rho_0}\frac{\partial P'}{\partial x_i} + \mathrm{RU}_i, \tag{19}$$

$$\frac{\partial P'}{\partial t} = +\gamma P_0 \frac{\partial \bar{U}_j}{\partial x_j} + \mathrm{RP}, \tag{20}$$

respectively, where RU_i and RP are the nonacoustic terms and $(1/\rho_0)\partial P'/\partial x_i$ and $\gamma P_0 \partial \bar{U}_j/\partial x_i$ are the acoustic terms. The leapfrog marching scheme is carried out on a large timestep Δt_L determined from meteorological phase speeds. A smaller timestep Δt_s is used for the acoustic terms in a "submarch," where $\Delta t_L = N\Delta t_s$ and N is some integer. The RU_i and RP terms are evaluated at the $\tau - N\Delta t_s$ time level for the diffusion terms and the τ level for advective and other terms. The acoustic terms are evaluated on a timestep Δt_s in a marching process between time levels $\tau - N\Delta t_s$ and $\tau + N\Delta t_s$ in timesteps of $2\Delta t_s$. This process appears as

$$\bar{U}_i^{[\tau - N\Delta t_s] + 2n\Delta t_s} = \bar{U}_i^{[\tau - N\Delta t_s] + 2(n-1)\Delta t_s} + 2\Delta t_s \times \left[\left(-\frac{1}{\rho_0}\frac{\partial P'}{\partial x_i} \right)^{[\tau - N\Delta t_s] + 2(n-1)\Delta t_s} + RU_i^{\tau, \tau - N\Delta t_s} \right], \tag{21}$$

$$P'^{[\tau - N\Delta t_s] + 2n\Delta t_s} = P'^{[\tau - N\Delta t_s] + 2(n-1)\Delta t_s} + 2\Delta t_s \times \left[\left(\gamma P_0 \frac{\partial \bar{U}_j}{\partial x_j} \right)^{[\tau - N\Delta t_s] + 2n\Delta t_s} + RP_i^{\tau, \tau - N\Delta t_s} \right], \tag{22}$$

where $n = 1, \ldots, N$ is the small time step iteration level.

Notice that a forward step on the diffusion terms and a leapfrog step on advective and other non-acoustic terms of $2\Delta t_L$ is completed after $2N$ small timesteps are taken. Note also the acoustic marching process is done in a semi-implicit manner using timesteps of $2\Delta t_s$, such that the divergence term in Eq. (22) is calculated as a function of the new time level of $\bar{U}_i$. This numerical procedure has been found to be neutrally stable by Klemp (personal communication) for the conventional CFL criteria for leapfrog on a 3D staggered grid given by

$$\sqrt{3} 2 C_s \Delta t_s / \Delta x \leqslant 1,$$

where C_s is the phase speed of the acoustic wave. The long timestep is bounded by a similar criterion for slower meteorological and internal gravity wave phase speeds.

In order to prevent solution separation which is common with the leapfrog scheme, a time smoother proposed by Robert (1966) has been introduced. Asselin (1972) analyzed the damping characteristics of this scheme and found it to have little impact on the physical modes. The modified leapfrog time-marching scheme is of the form

$$\left.\begin{aligned} u^{*\tau + \Delta t} &= u^{\tau - \Delta t} + \frac{\partial}{\partial t}(u^{*\tau}) 2\Delta t \\ u^{\tau} &= u^{*\tau} + \tfrac{1}{2}k(u^{*\tau + \Delta t} - 2u^{*\tau} + u^{\tau - \Delta t}) \end{aligned}\right\}, \tag{23}$$

where k (a damping coefficient) is set to 0.2, τ is the time level and Δt the timestep. This scheme was applied on the long timestep integration only.

The time-split compressible model has been benchmarked against a fully explicit compressible model employing the modified leapfrog time marching scheme iterated at the small timestep Δt_s on all prognostic variables. The bench test was first performed in two dimensions for a moist cloud simulation similar to that described in Section 6. Data predicted by the time-split compressible model and the explicit compressible model were compared through 15 min of simulated time. No significant differences could be seen in the predicted fields of motion or the water content and temperature fields. Occasionally, significant differences appeared at individual grid points due to slight differences in propagation of the cloudy disturbance. Such differences may be attributed to differential truncation error. A comparative test was also made in three dimensions but only for a total simulated time of 3 min. The results of the test were consistent with the two-dimensional evaluation.

d. Boundary conditions

Lateral boundaries were specified for all variables from their large-scale values and held constant through the integration. Both upper and lower boundaries are given to be rigid walls by setting $u_3 = 0$. The eddy diffusion terms are set

$$-\overline{u_3'' A''} = 0$$

for $\bar{A} = \bar{u}$, $\bar{v}$, $\bar{P}'$, $\bar{\theta}$, $\bar{q}_v$, $\bar{Q}_c$ on the top and bottom boundaries.

3. Description of the case study

In order to facilitate comparison of the numerical simulation experiments discussed in the following

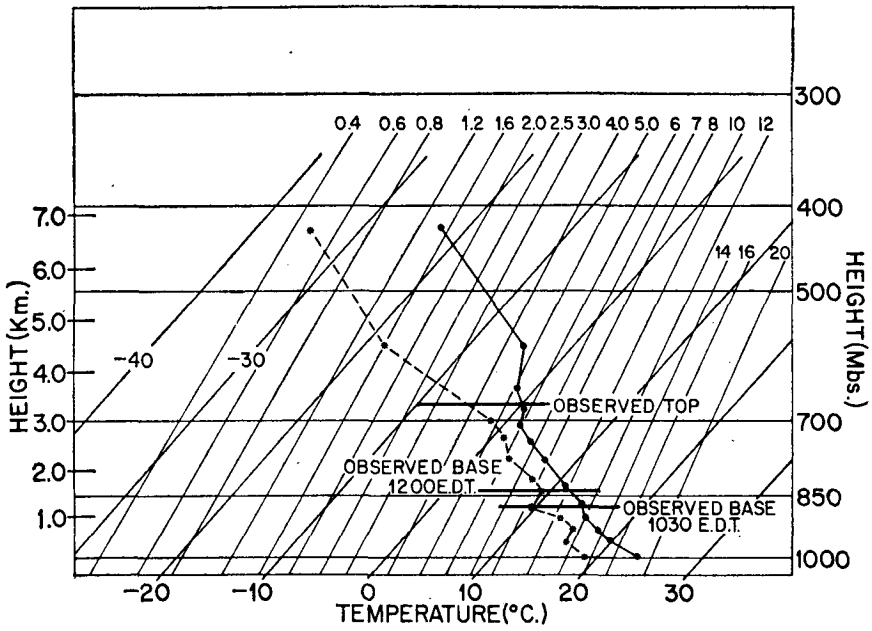

FIG. 1. Observed aircraft sounding taken 1146–1215 EDT at Bundaberg, Queensland, to 680 mb, patched with the Brisbane 2300 GMT sounding above 680 mb, for 10 November 1964.

sections with those previously reported by Cotton (1975), the same case-study data are used throughout. A detailed discussion of the 10 November 1964 observations made by J. Warner (Head of the Cloud Physics Group of CSIRO at Sydney) over Bundaberg, Queensland, are reported in Cotton (1975). Therefore, only a few features will be described here. Fig. 1 illustrates the thermodynamic sounding observed by aircraft up to 680 mb from 1146–1215 EDT, patched with the Brisbane 2300 GMT (0900 EDT) sounding above 680 mb, for 10 November 1964. The main cloud layer is conditionally unstable with a temperature lapse of 7°C km^{-1} which is capped by a stable layer with a temperature lapse of 5.50°C km^{-1}.

Fig. 2 illustrates the wind profile observed by pilot balloons from the Bundaberg airport at 1145 EDT. Below 1500 m the winds were generally out of the northeast at 5.8–7.4 m s^{-1}. At 1800 m the winds were light and variable. Above 3000 m the winds became southerly at speeds over 6.8 m s^{-1}. The vertical shear of the horizontal wind between 1000 and 2000 m was on the order of 1.2×10^{-3} s^{-1} and increased to 7.7×10^{-3} s^{-1} between 2000 and 3000 m. Because the one-dimensional models used by Cotton (1975) do not respond to horizontal wind or its shear, these observations were not reported in that work.

Warner (personal communication) reported cumulus tops were observed at ~3.4 km. Cloud bases were observed at 1.22 km at 1030 EDT rising to 1.55 km at 1200 EDT. Aircraft cloud penetrations were begun at 1010 EDT at an altitude of 2.77 km MSL, followed by penetrations at altitudes 2.34, 1.9 and 1.5 km. Table 1 summarizes the observed $\bar{Q}_c$, $\bar{Q}_c/Q_A$ and $\bar{w}$ at the four observation levels where the average is computed over a constant horizontal scale corresponding to the visible cloud diameter at 1.5 km. As mentioned by Cotton, the values of $\bar{Q}_c/Q_A$ computed from this case study corresponded to Warner's mean profile at 360 and 800 m above cloud base. At the top-most observation level (1230 m above cloud base), however, the computed value of $\bar{Q}_c/Q_A$ from this case study was 0.275, whereas Warner's mean profile of $\bar{Q}_c/Q_A$ gives a value of 0.2 at that level. Still the difference between Warner's mean profile and the computed $\bar{Q}_c/Q_A$ for this case study is relatively small. Also shown in Table 1 is the computed vertical velocity averaged over the cloud diameter at the four observation levels. The computed $\bar{w}$ ranged from near zero at cloud base to 3.65 m s^{-1} at 1230 m above cloud base and exhibited a secondary maximum of 2.88 m s at 360 m above cloud base. The reader is referred to Cotton (1975) for a further description of the aircraft observations.

As was mentioned by Cotton (1975), the major shortcoming in this observation is the lack of documentation of the nature of the subcloud structure, including surface temperature, orography, vertical turbulent fluxes of heat, moisture and momentum, or mesoscale convergence. The lack of these observations severely limits the ability to unambiguously verify the predictions of multidimensional cloud models. Unfortunately, there are virtually no reported, simultaneous observations of detailed cumulus cloud structure and its subcloud structure.

Because of this uncertainty, the numerical experi-

ments to be described in the following sections will be initiated by a moist bubble of air having a zero temperature anomaly. Above the observed cloud base, the air is assumed to be saturated through a depth of twice the observed cloud height and over a horizontal extent equal to the cloud diameter. Below cloud base, the moisture anomaly linearly decreases from the saturated value at cloud base at the cloud center to zero at a distance equal to the cloud radius. As compared to a combined saturated moisture anomaly and a temperature anomaly that many modelers have used, this moisture perturbation is relatively weak in magnitude. Still, this represents a very unrealistic means of initiating a cumulus cloud. The main virtue of using such a moisture perturbation is that it allows us to compare the data predicted by the three-dimensional model with the data predicted by the one-dimensional model reported by Cotton (1975). The latter models were initiated with a moisture anomaly of a similar nature.

4. Philosophy of comparison of model predictions with observations

As was pointed out in Section 1 and can be seen from our description of the case study, the observed data are far too sparse to provide an adequate basis for verifying the predictions of a 3D model. Differences between the model predicted parameters and observed parameters could not only be attributed to model forecast errors but also to errors or uncertainties associated with cloud formative processes (i.e., boundary layer processes and mesoscale systems) and to time variations in cloud parameters during the period of observation. Use of the available observed data to initialize a model as well as to compare with the model predicted data does restrict the degrees of freedom available to the modeler, however. Thus if the model does not significantly overpredict or underpredict the observed cloud top heights, liquid water contents or air velocity fields, one has greater confidence that the conclusions that are drawn from the numerical experiments are meteorologically meaningful.

One can better make the comparison of model predictions with observations by choosing observed parameters which exhibit some spatial and temporal consistency. Warner (1970a) chose $\bar{Q}_c/Q_A$ for model comparison because it provides a means of normalizing a large body of data and, furthermore, it exhibited a consistent trend of decreasing as a function of height above cloud base (z_b). As can be seen in Table 1, the observed $\bar{Q}_c/Q_A$ obtained from an individual case study does not differ appreciably from Warner's mean profile. The greatest departure from Warner's mean profile occurs at the uppermost and first observation level. Because Warner began his aircraft penetrations in actively rising towers, the data shown in Table 1 suggests that the tops of the actively rising towers

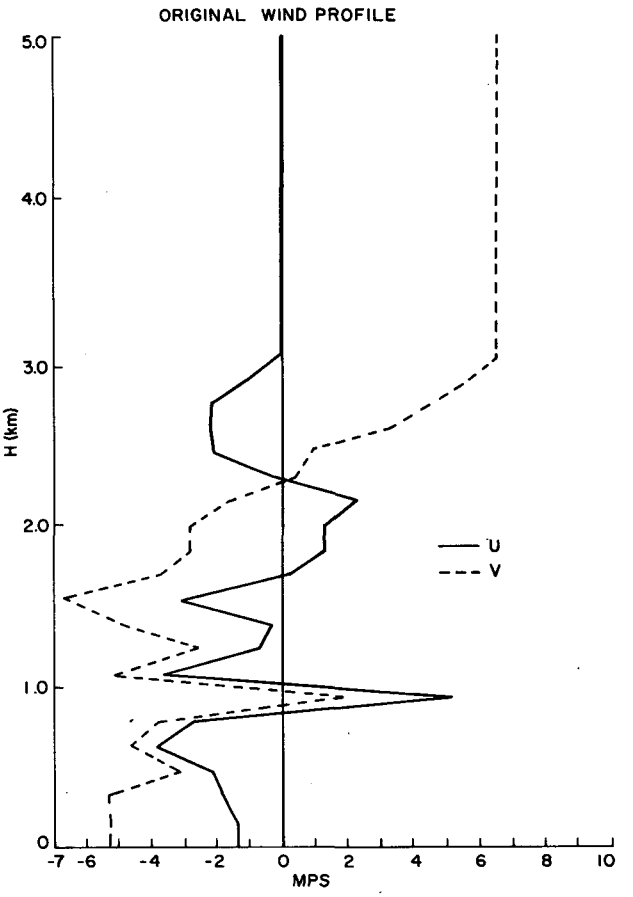

FIG. 2. Wind profile observed by pilot balloons from the Bundaberg airport at 1145 EDT.

exhibit slightly higher values of $\bar{Q}_c/Q_A$ at a given height above cloud base than the main body of the cloud. Warner's mean profile of $\bar{Q}_c/Q_A$ as a function of z_b can then be considered to be composed of a few penetrations in the tops of the rising towers with the majority of the contributions coming from penetrations in the main body of the clouds.

While analyzing the $\bar{Q}_c/Q_A$ profiles predicted with the 1DTD model, Cotton found that the model developed a single "bubblelike" solution with the highest values of $\bar{Q}_c/Q_A$ at a given z_b occurring shortly after

TABLE 1. Observed cloud parameters. Properties averaged over the main cloud diameter corresponding to 490 m.

Height (m)	Run no.	$\bar{Q}_c$ (g kg^{-1})	$\bar{Q}_c/Q_A$	$\bar{w}$ (m s^{-1})	Height above cloud base (m)
1500	4	0.08	—	0.09	—
1900	3	0.30	0.43	2.88	360
2340	2	0.38	0.24	1.56	800
2700	1	0.66	0.275	3.65	1230

the bubble passed a given z_b and rapidly decayed in time thereafter. Associated with the decay in the magnitude of $\bar{Q}_c/Q_A$ with time was a rapid rise in the height of cloud base. As pointed out earlier, Warner observed the cloud bases to rise during the period of observation. The rate of rise of the cloud base predicted by the 1DTD, however, was much faster than the observed rise rate. This was attributed to the unrealistic nature of the initial moisture anomaly. Rather than "fiddle" with the unknown surface conditions (i.e., surface temperature, surface moisture, low-level convergence), until a reasonable cloud-base rise rate was obtained, it was decided to stick with this initialization method. The predicted peak values of $\bar{Q}_c/Q_A$ at a given z_b (where z_b is defined as the height above the observed initial cloud-base height) were compared with the $\bar{Q}_c/Q_A$ computed from the case-study data and with Warner's mean profile of $\bar{Q}_c/Q_A$. While the predicted peak values of $\bar{Q}_c/Q_A$ may be expected to be higher than Warner's mean profile of $\bar{Q}_c/Q_A$, the observed case-study data shown in Table 1 suggest that the differences would not be excessive. Because the 3D model cloud simulations also developed single "bubble-like" solutions in response to a moisture anomaly similar to that used with the 1DTD model, the peak magnitudes of $\bar{Q}_c/Q_A$ predicted at a given z_b with this model will also be compared with the observed case-study data and Warner's mean profile of $\bar{Q}_c/Q_A$. In addition, the instantaneous profile of $\bar{Q}_c/Q_A$ as a function of z_b predicted with the 3D model will be compared with Warner's mean profile.

It is also desirable to compare other simulated cloud parameters such as vertical velocity (w) with the observed case-study data. Warner (1970b) has shown, however, that the vertical velocity averaged over the width of the cloud shows no consistent change with height. Warner (1977) also suggested that the vertical velocity averaged over the width of the cloud varies strongly with time at any given level. In contrast with $\bar{Q}_c/Q_A$, it therefore becomes extremely difficult to make an unambiguous comparison between model predictions and aircraft observations of cloud-scale averaged vertical velocity. We will, therefore, present the model-simulated vertical velocity averaged over saturated grid points mainly for comparison between models.

We might have selected the rms vertical velocity averaged over the cloud width or the peak updraft and downdraft magnitudes as parameters to be used for comparison with observations. Warner (1970b) showed these parameters generally increase with height. Unfortunately, since the selected horizontal grid resolution is only sufficient to represent four or five grid points across the cloud at any given level, meaningful rms velocities or peak velocities cannot be expected to be predicted by the model. This is especially true of vertical velocity since the aircraft-observed w field illustrated in Cotton (1975) exhibits strong fluctuations on the scale of tens of meters. At the same time the numerical experiments described by Lipps (1977) and Klemp and Wilhelmson (1978) indicate that the deformation eddy viscosity model used in this study significantly underestimates the subgrid-scale contribution to the rms velocities. Thus, these predicted parameters will not be compared with the observed data in this study.

5. Results of a three-dimensional cloud simulation in a no-motion environment

a. The predicted flow field

The first numerical experiment to be described here is for the case of an assumed zero-horizontal-wind field. The only asymmetric forcing in the experiment is due to the weak Coriolis term in (1). Therefore, this calculation can be directly compared with the previously reported 1DL and 1DTD model solutions. It can also be compared with two-dimensional, axially symmetric models reported by other workers.

Fig. 3 illustrates the predicted circulation field after 450 s of simulated time. In response to the moisture anomaly, the model predicts a thermal-like cloud element with a characteristic toroidal circulation. The toroidal circulation has also been obtained in the two-dimensional, axi-symmetric cloud simulations of

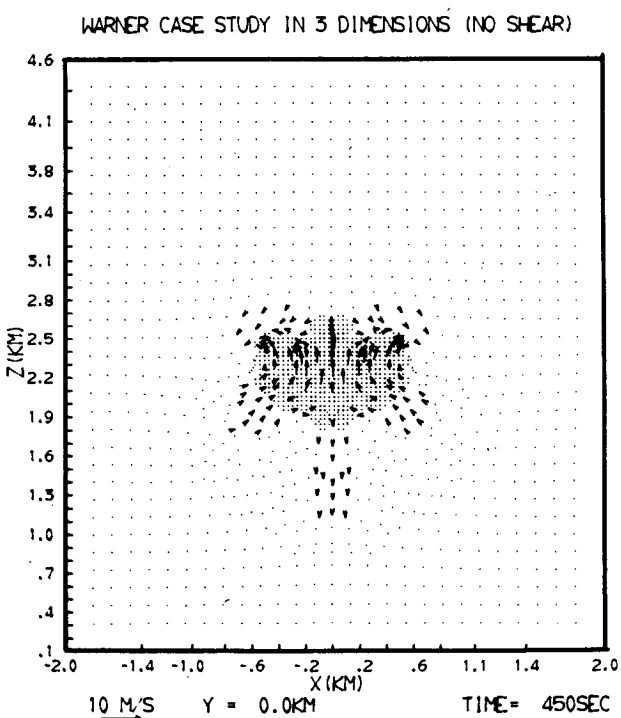

FIG. 3. East–west vertical cross section of vector wind field and cloud water as predicted by 3D model with no mean motion imposed. Shaded areas represent areas in which cloud water exists. The section is taken at the initial perturbation center. Grid point locations are indicated by tick marks along the axis.

Ogura (1963), Murray (1970) and Soong and Ogura (1973). Similar to the results of numerical experiments with the 1DTD model reported by Cotton (1975), the simulated cloud base rises with time. A weak downdraft can be seen in the region immediately below the cloudy bubble. The downdraft is created by the evaporation and subsequent chilling of the cloudy residue left in the wake of the rising bubble. Fig. 4 illustrates the predicted pressure perturbation field at 450 s. A weak low pressure anomaly on the order of 0.04 mb exists in the main body of the cloud with an even weaker high pressure anomaly above cloud top. The highest magnitude pressure anomaly was predicted in the region of the chilled cloud residue below the rising bubble. Even this anomaly was only +0.052 mb.

After 510 s of simulated time, the cloud begins to separate and develop a downdraft. Downdrafts within non-precipitating clouds are not at all surprising. One of us (WRC) has experienced a downdraft in excess of 18 m s^{-1} while flying with Warner through clouds of similar stature near Bundaberg, Queensland. The splitting of the simulated cloud illustrated in Fig. 5 at 600 s is explained by strong convergence in the lower portion of the cell which has led to what Murray (1970) has called "dynamic entrainment" of relatively dry air. The entrained dry air causes evaporational cooling in the lower portion of the cloud and hence a region of negative buoyancy ($\theta' = -1$ to -2°C). The upper portion of the cloud, on the other hand, has remained positively buoyant ($\theta' = 2$–2.5°C) through the continued release of latent heat and the detrainment of cloudy

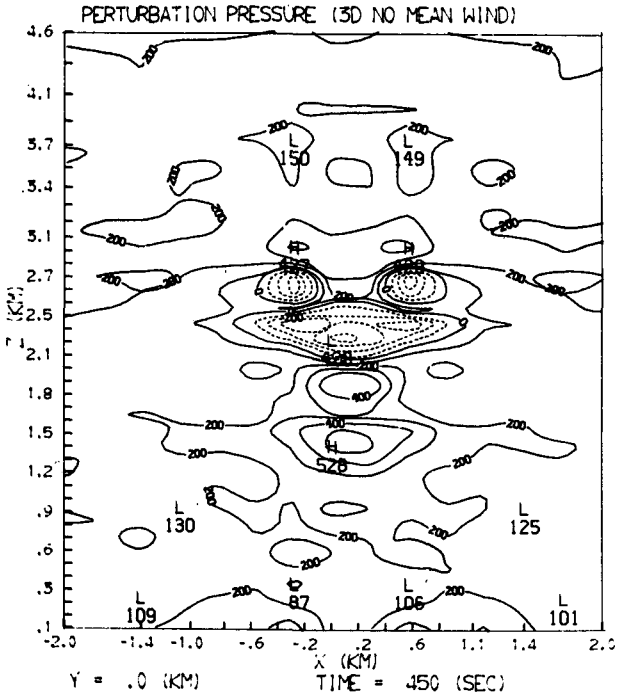

FIG. 4. Pressure perturbation field corresponding to wind field depicted in Fig. 3. Labels are mb $\times 10^5$.

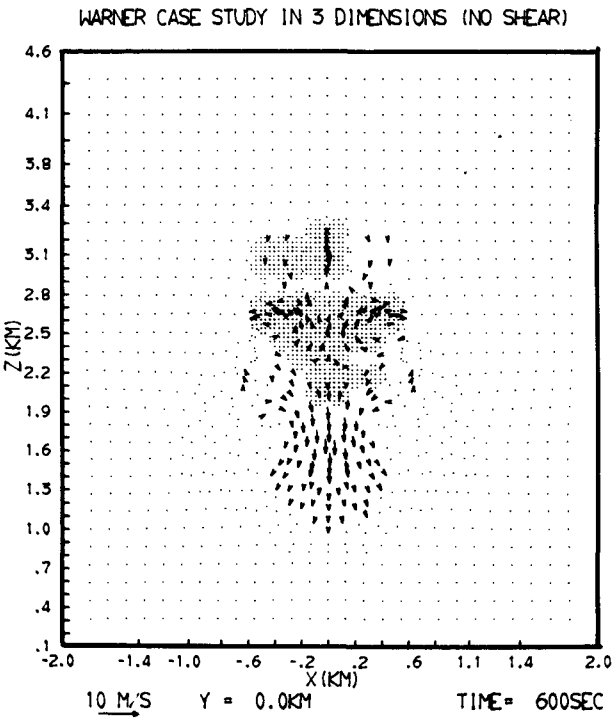

FIG. 5. As in Fig. 4 except time is 600 s.

air. The detraining region or region of divergence prevents the cloud interior from being mixed with environmental air. As a result the upper portion of the cloud rises faster than the lower portion creating a separation between the two cloud areas.

It should be noted that the eddy viscosity turbulence parameterization [Eqs. (12) and (13)] also contributes to the total cloud entrainment, but the predicted turbulent flux divergences are generally three to four orders of magnitude smaller than the mean advective flux divergences. This is consistent with the two-dimensional, axi-symmetric model results of Murray (1970) and Ogura (1963), who also found that the explicitly represented motions generally dominated the bulk entrainment of the simulated cloud.

A slight asymmetry can be seen in the motion field and the saturated region illustrated in Fig. 5. This is a consequence of retaining the Coriolis terms in (1).

b. The predicted profile of $\bar{Q}_c/Q_A$

As a means of quantifying the bulk effects of entrainment, the average cloud liquid water content $\bar{Q}_c$ over the saturated grid points at each level was computed. The ratio $\bar{Q}_c/Q_A$ was then computed at each level, where Q_A was predicted with the respect to the initial cloud-base temperature. The predicted time variation of $\bar{Q}_c/Q_A$ shown in Fig. 6 has remarkable similarity to the profiles predicted by the 1DTD model shown in Cotton (1975). Most noteworthy is that both models predict a characteristic packing of the contours of

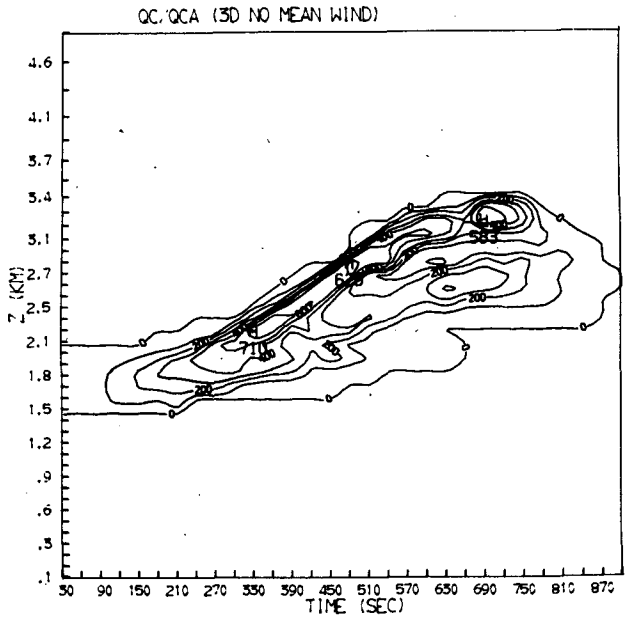

FIG. 6. Predicted profile of $\bar{Q}_c/Q_A$ for the 3D no-mean motion experiment. Labels are g g$^{-1}\times 10^3$.

$\bar{Q}_c/Q_A$ near the top of the rising cloud element. A troublesome feature illustrated in Fig. 6 is that a vertical sounding of $\bar{Q}_c/Q_A$ at any particular time exhibits $\bar{Q}_c/Q_A$ increasing with height above cloud base. Such a profile is quite inconsistent with the mean $\bar{Q}_c/Q_A$ profiles reported by Warner (1970a), which exhibit a sharp drop in the magnitude of $\bar{Q}_c/Q_A$ as a function of height in the first kilometer above cloud base, followed by a nearly constant magnitude of approximately 0.2 at higher levels. The computed $\bar{Q}_c/Q_A$ observed for this case study (see Table 1) also exhibits a sharp fall in magnitude at the first two observation levels but with a slightly higher magnitude at the uppermost observational level compared to the one immediately below. Nonetheless, the predicted increase in $\bar{Q}_c/Q_A$ as a function of height at any particular time far exceeds the observed magnitudes.

If we confine our attention to comparing the peak predicted magnitude of $\bar{Q}_c/Q_A$ by the three-dimensional model at a given z_b against those observed in this case study, the discrepancy becomes very large at the highest levels. The magnitude of $\bar{Q}_c/Q_A$ predicted at 1.9 km MSL had peak values ranging from 0.45 to 0.49, which is slightly higher than the observed value of 0.43. At 2.34 km MSL, the 3D model predicted peak values of $\bar{Q}_c/Q_A$ ranging from 0.59 to 0.73, while the observed magnitude was as low as 0.24. At the uppermost observation level (2.77 km MSL) the observed $\bar{Q}_c/Q_A$ was 0.275, while the peak magnitudes predicted were as high as 0.67. Certainly, it does not appear that the 3D model eliminates the discrepancy between observed and predicted profiles of $\bar{Q}_c/Q_A$ in any way. In fact, the peak values of $\bar{Q}_c/Q_A$ predicted by the three-dimensional model are even higher in magnitude at the uppermost levels than those predicted by the 1DTD model.

On the other hand, the cloud top heights predicted by the 3D model agreed quite well with observations. The predicted top was 3.35 km, while the observed top was 3.4 km MSL. It may be expected then that any attempts to improve entrainment predictions by adjusting the eddy exchange coefficients or subcloud fluxes could only adversely affect the cloud-top height prediction. This result is indeed disturbing, since the 3D model explicitly predicts the cloud circulation on a 200 m horizontal grid including the effects of perturbation pressure gradients. The predicted mean horizontal motion in the 1DTD model, on the other hand, is diagnosed from the continuity equation averaged over the cloud radius (~400 m) and the effects of pressure gradients are ignored. One common feature between the two models is that both models employ an eddy-viscosity parameterization [Eqs. (12) and (13)]. Cotton (1975) suggested that perhaps the use of such a first-order turbulence model could force a greater fraction of the cloud fluxes, on the mean field, thus accounting for large values of $\bar{Q}_c/Q_A$. Another common feature between the 1DTD model and the 3D model numerical simulation described above is that neither model responds to the effects of the large-scale wind. We will explore this factor in Section 6b. Before we do so, however, we will compare the vertical velocity (w) field predicted with the 3D model with the observed magnitudes.

Fig. 7 illustrates the time variation of predicted

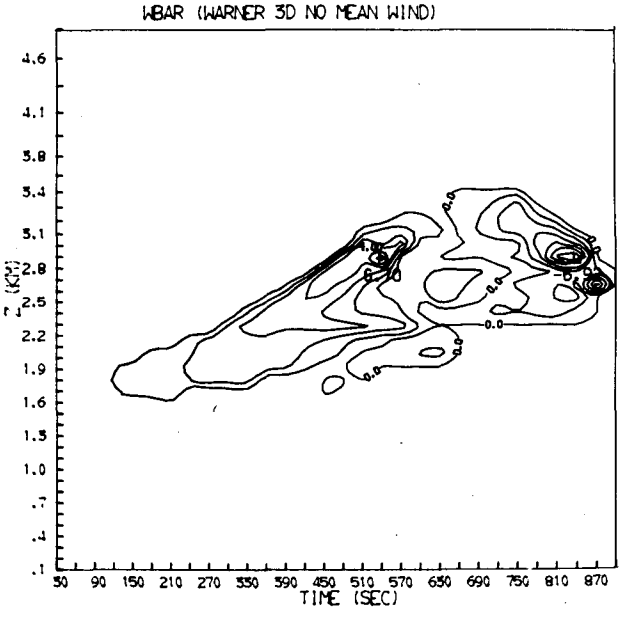

FIG. 7. $\bar{w}$ predicted by 3D no-mean motion experiment. Labels are in m s^{-1}.

vertical velocity averaged over saturated grid points. The profile of $\bar{w}$ is quite similar to that predicted by the 1DTD model by Cotton (1975). The maximum $\bar{w}$ predicted by the 1DTD model, however, exceeded 6 m s^{-1}, while the maximum $\bar{w}$ predicted by the 3D model was 6.7 m s^{-1}. Inspection of Table 1 illustrates that the peak $\bar{w}$ predicted with the 3D model exceeded the observed $\bar{w}$ at the top two observation levels by 0.9 and 2.1 m s^{-1}, respectively. At 1900 m, however, the peak predicted $\bar{w}$ was comparable to the observed magnitude. At the 1500 m level the peak predicted $\bar{w}$ was generally much larger than the observed value. It is also interesting to note that the maximum value of the predicted average downdraft exceeded the average updraft. This occurred during the final dissipation of the cloud.

6. Results of a three-dimensional cloud simulation in shear flow

a. *The predicted flow field*

The second numerical experiment is designed to determine the importance of the observed wind field on the predicted cloud circulation and such parameters at $\bar{Q}_c/Q_A$. In order to limit the domain of simulation (keep the cloud in a small box as long as possible), the mean wind through the cloudy layer from 1.0 to 2.0 km was removed from the wind profile. The wind profile was also smoothed using a 1-2-1 filter. Fig. 8 illustrates the smoothed wind profile with the mean in the layer between 1.0 and 2.0 km removed. It should also be noted that the Coriolis terms in (1) were computed with respect to the total wind velocities, whereas all remaining terms were evaluated with the mean removed from the wind profile.

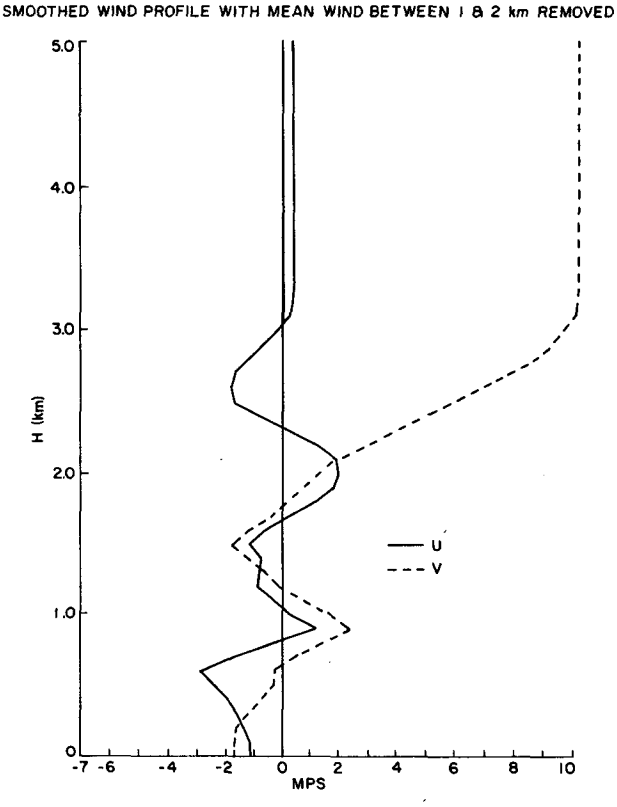

FIG. 8. Observed wind profile smoothed with a 1-2-1 smoother and with the mean between 1.0 and 2.0 km removed.

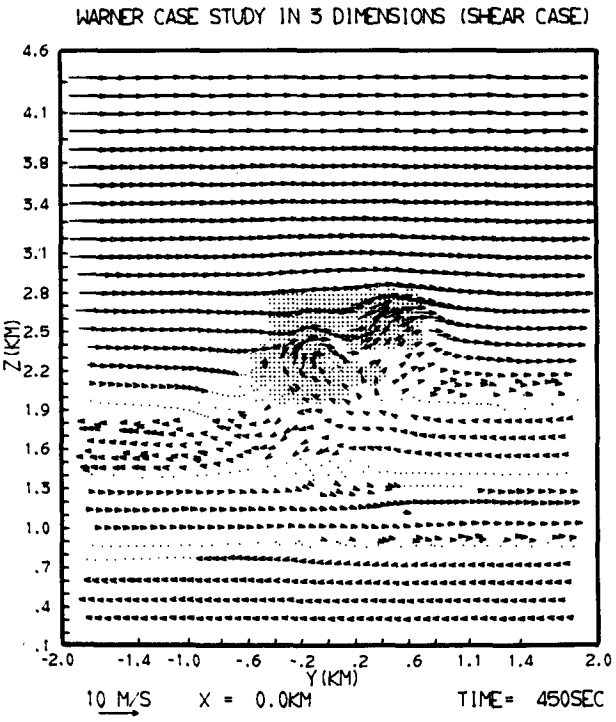

FIG. 9. North–south vertical cross section of vector wind field and cloud water as predicted by 3D model assuming a mean sheared wind profile. Section taken at initial perturbation center.

In contrast to the no-motion (zero mean wind) experiment discussed above, a number of interesting and unique features of the cloud circulation were predicted. Fig. 9 illustrates the simulated wind field and cloud region (dotted area) after 450 s of time. The figure is a north–south cross section, which is the plane of maximum shear. During its most active stage of growth, the cloud remained relatively erect, even though the tower was penetrating into the shear layer.

The circulation in the saturated region is distinctly different in character from the perfectly symmetrical circulation in the no-motion simulation. Most evident is the dominance of a single circulation cell in contrast to the pair of oppositely rotating cells which were a feature of the no-motion simulation. The perturbation pressure field shown in Fig. 10 likewise exhibited the asymmetry of the cloud dynamics. In this case the major pressure anomalies are either in the saturated regions or immediately above the cloud. The upstream edge of the cloud was characterized by positive pressure anomalies as large as 0.06 mb, while the downstream

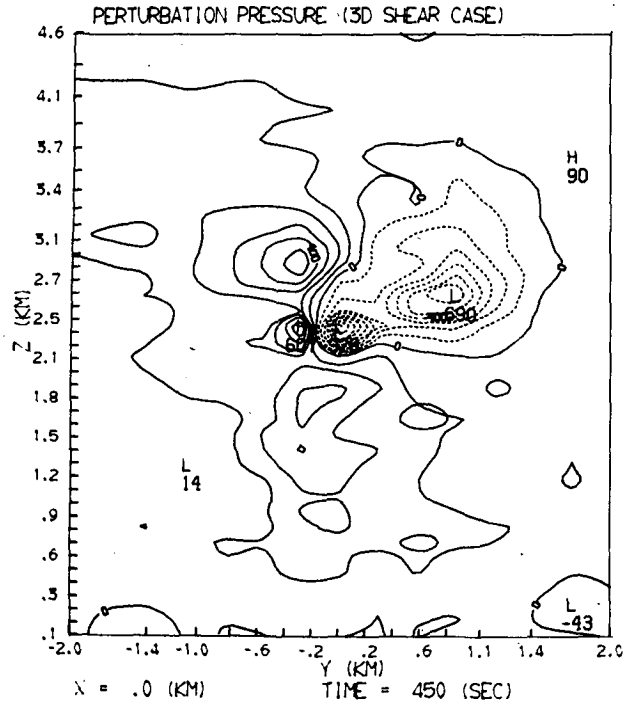

FIG. 10. Perturbation pressure field corresponding to wind field depicted in Fig. 9.

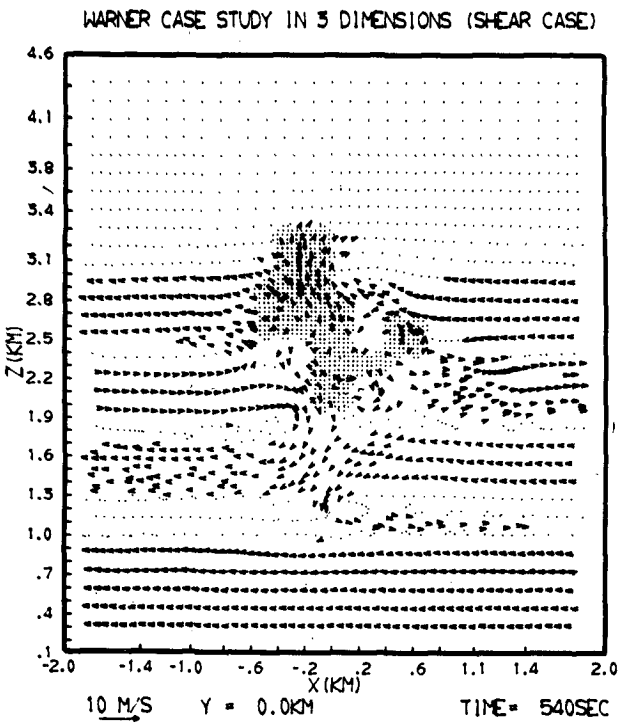

FIG. 12. East–west vertical cross section of wind field and cloud water for the 3D experiment assuming a mean sheared wind profile. Section at initial perturbation center.

portions of the cloud had negative anomalies as large as 0.092 and extended a considerable distance downwind. The magnitude of the predicted maximum pressure anomaly at 450 s in the shear-flow simulation was nearly twice that predicted in the no-motion simulation.

As illustrated in Fig. 11, by 600 s the simulated

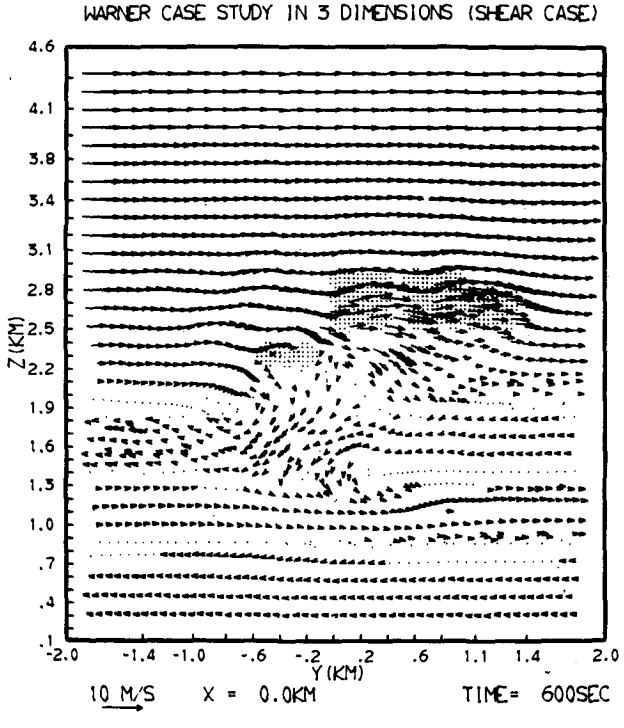

FIG. 11. As in Fig. 10 except at 600 s.

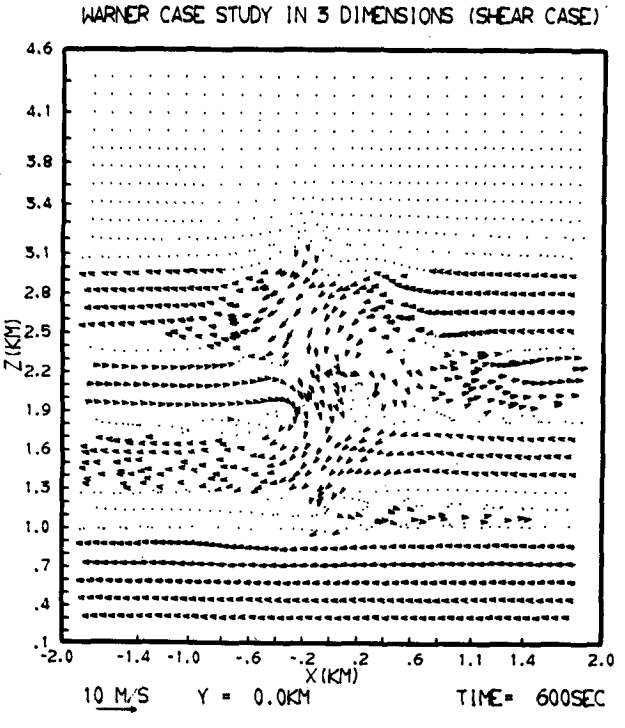

FIG. 13. As in Fig. 12 except at 600 s.

cloud was noticeably affected by the shear flow. The upper portion of the cloud was blown downstream relative to the lower region. At. 2.5 km MSL the entrainment of the higher momentum air was causing a visible separation of the cloud. While the toroidal circulation in the no-motion simulation also caused a cloud separation, the shear-flow definitely caused a more rapid decay of the cloud circulation. The character of the downdraft was also altered by interaction with the shear flow. In this case, the downdraft was concentrated in the upshear side of the cloud. Presumably, if the cloud were growing from an active planetary boundary layer circulation, the laterally displaced downdraft would provide the impetus for new tower growth on the upshear side of the cloud.

Fig. 12 illustrates a projection in the east–west plane or the plane having relatively low wind speeds but which are variable in direction. At 540 s the cloud appears to be in the process of being rapidly eroded away at low levels. Above 2.5 km MSL, a rather active tower remains, however. By 600 s, the cloud shown in Fig. 13 has completely disappeared from this plane leaving a deep downdraft region. Moving northward 800 m, however, the projection at 600 s still contains a vigorous cloud circulation. A curious feature is the presence of a weak downdraft at the very top of the saturated region.

The predicted horizontal map at a height of 1.9 km MSL after 300 s is shown in Fig. 14. The complex nature of the interaction of the cloud motion field and the environmental wind field is illustrated by the formation of a weak flow in the upwind portion of the cloud interior which has a direction nearly perpendicular to the mean flow. The corresponding predicted pressure anomaly (Fig. 15) is surprisingly smooth with a broad high pressure region in the upwind portion of the cloud extending around its right flank. The main body of the cloud is characterized by a broad nearly symmetric region of low pressure with a peak amplitude of 0.047 mb.

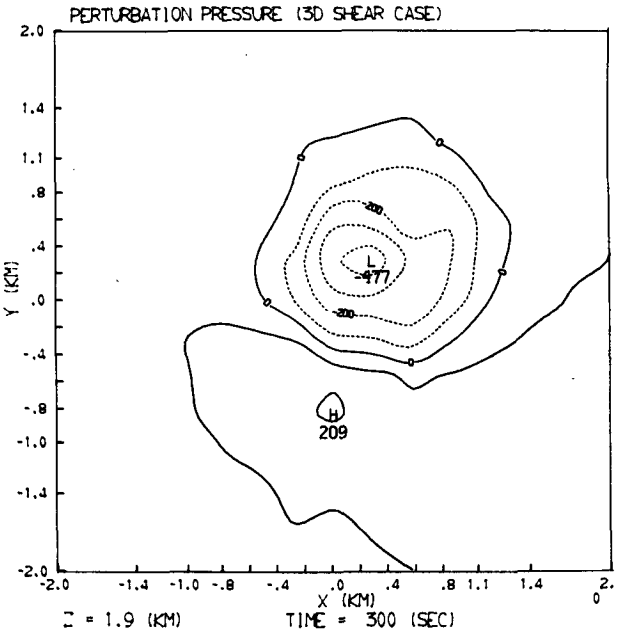

FIG. 15. Perturbation pressure field corresponding to flow field depicted in Fig. 14. Labels are 10^5 mb.

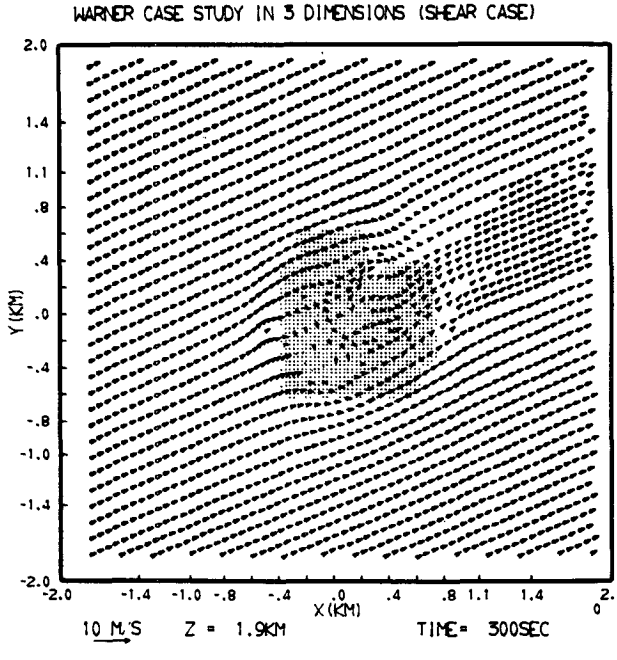

FIG. 14. Horizontal cross-section at initial perturbation top (1.95 km MSL) of wind field and cloud water for 3D experiment assuming a mean sheared wind profile.

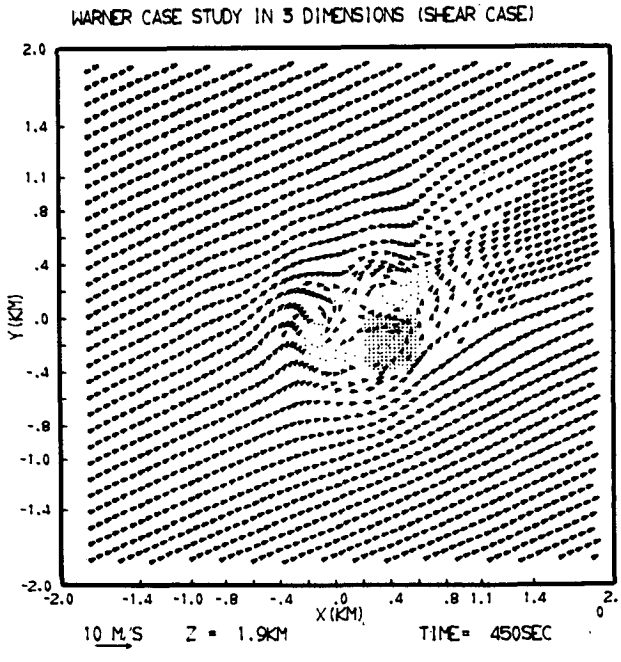

FIG. 16. As in Fig. 15 except at 450 s.

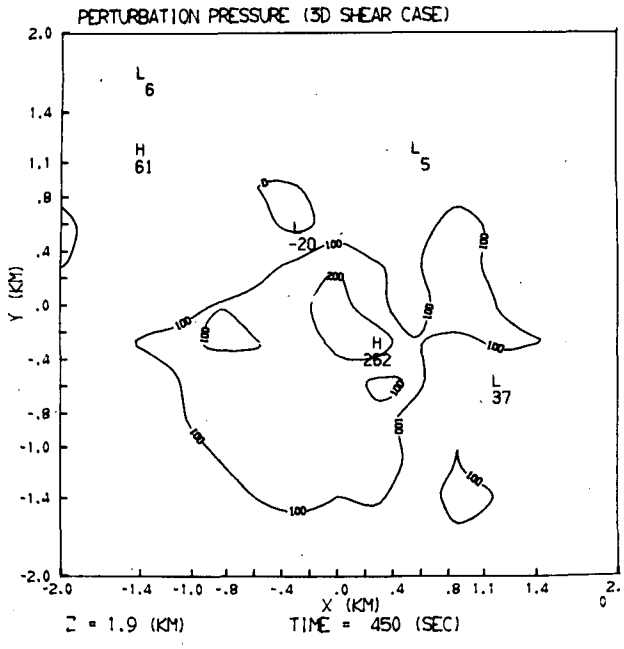

FIG. 17. Perturbation pressure field corresponding to flow field depicted in Fig. 16. Labels are 10^5 mb.

As shown in Fig. 16, the cloud nearly passed through the 1.9 km level by 450 s. The horizontal circulation field had become quite complex by this time with a vortex doublet present in the downstream portion of the cloud. This feature is somewhat reminiscent of the vortex doublet simulated by Schlesinger (1975) in a severe storm simulation. A weak cyclonic circulation (remember this is a Southern Hemispheric simulation) can also be seen in the left upstream flank of the cloud. The predicted pressure perturbation field (Fig. 17) at this time had become quite disorganized. The largest pressure anomaly was a positive anomaly on the order of 0.026 mb in the upstream edge of the cloud. Since this calculation was performed with Coriolis terms included in (1), one might ask whether or not these terms significantly contributed to the formation of the weak vortices. The numerical experiment was thus repeated with the Coriolis terms set equal to zero. Results show that the vortices are not formed as a consequence of the earth's rotation but instead they are a result of the interaction of the cloud momentum field with an environment exhibiting both directional and speed shear of the horizontal wind.

b. The predicted profile of $\bar{Q}_c/Q_A$

In order to investigate the effects of shear on the bulk properties of a cloud, the ratio $\bar{Q}_c/Q_A$ predicted by the model was computed. The average liquid water content $\bar{Q}_c$ was again computed over all saturated grid points at a given level. Fig. 18 illustrates the predicted time variation of $\bar{Q}_c/Q_A$ for the three-dimensional, shear-flow numerical experiment. The first noteworthy feature is that the strong packing of the contours of maximum $\bar{Q}_c/Q_A$ near cloud top which so characterized both the 1DTD and 3D no-motion simulations is virtually non-existent in the shear-flow simulation. Correspondingly, vertical soundings of $\bar{Q}_c/Q_A$ early in the life cycle of the simulated cloud exhibit a sharp lapse in the magnitude of $\bar{Q}_c/Q_A$ with values at upper levels on the order of 0.2. Later in time the soundings exhibit a tendency for $\bar{Q}_c/Q_A$ to increase with height but the magnitudes are considerably smaller than those predicted by either the 1DTD or the 3D no-motion simulations.

Comparing the predicted $\bar{Q}_c/Q_A$ with observations at 1.9 km MSL, we note that the peak predicted values of $\bar{Q}_c/Q_A$ are in the range 0.38 to 0.40, which are slightly lower than the 0.45 magnitude observed. This is also considerably lower than any of the magnitudes at this level predicted by the 1DTD or 3D no-motion simulations.

At 2.34 km MSL, the predicted values ranged as high as 0.35–0.45 which are somewhat higher than the 0.24 magnitude observed, but still better than any of the previously discussed model predictions.

At 2.77 km MSL, the peak predicted values of $\bar{Q}_c/Q_A$ ranged from 0.22 to 0.24, which is slightly lower than the observed value of 0.275. Overall these results are in far better agreement with the observed magnitude of $\bar{Q}_c/Q_A$ than predicted by the 3D no-motion simulation and the 1DTD and 1DT models.

Interestingly enough, the predicted cloud-top height in the shear flow experiment was 3.35 km which is in good agreement with the 3.4 km observed cloud-top height and identical with the top height predicted in the no-motion simulation. Thus while the interaction of

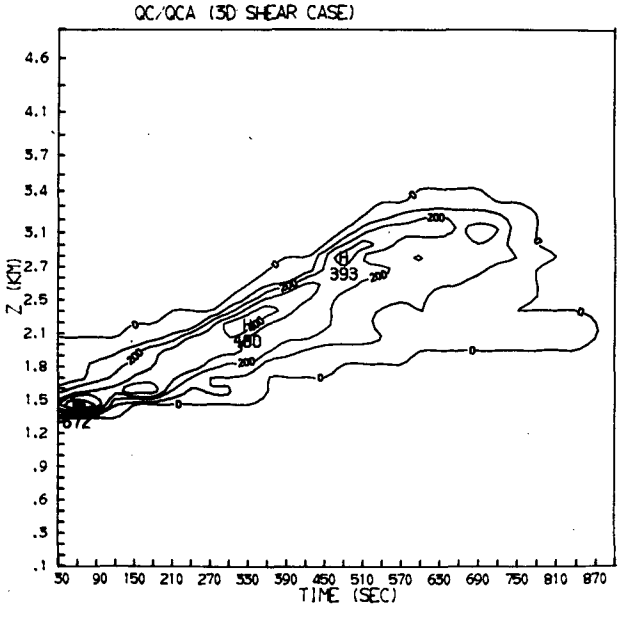

FIG. 18. $\bar{Q}_c/Q_A$ profile for 3D experiment assuming a mean sheared wind profile. Values are in g $g^{-1} \times 10^3$.

the cloud with an environment exhibiting vertical shear of the horizontal wind had a major influence on the prediction of cloud liquid water content, it had virtually no influence on the prediction of cloud top height.

c. The predicted vertical velocity field

Fig. 19 illustrates the predicted vertical velocity averaged over saturated grid points for the 3D shear-flow simulation. In contrast to the 3D, no-motion simulation, the predicted $\bar{w}$ for the 3D shear-flow simulation is considerably weaker in magnitude. The predicted maximum $\bar{w}$ for the 3D, no-motion simulation is more than 2.5 m s^{-1} greater than that predicted in the shear-flow simulation. It thus can be seen that, while shear flow has a relatively minor influence on predicted cloud top height, it has a major influence on the prediction of both $\bar{Q}_c/Q_A$ and $\bar{w}$.

Comparison of the predicted $\bar{w}$ with observations again illustrates the variable nature of the observed $\bar{w}$. At 1.5 km MSL the observed $\bar{w}$ was 0.09 m s^{-1} while the predicted $\bar{w}$ ranged from 0.2 to 0.9 m s^{-1}. At 1.9 km MSL the observed $\bar{w}$ was 2.88 m s^{-1}, while the predicted maximum $\bar{w}$ was 2.7 m s^{-1}. At 2.34 km MSL the observed $\bar{w}$ was 1.56 m s^{-1} while the maximum $\bar{w}$ predicted was 3.2 m s^{-1}, over 1.6 m s^{-1} greater. At 2.77 km MSL, the observed $\bar{w}$ was 3.65 m s^{-1} while the predicted maximum $\bar{w}$ had a smaller magnitude of 2.5 m s^{-1}. Thus the predicted $\bar{w}$ for the 3D shear flow simulation was neither consistently greater than nor less than observed values. In general, the magnitude of $\bar{w}$ predicted in the 3D shear flow simulation was closer to the observed values than in the no-motion simulation. The results, however, can by no means be considered definitive.

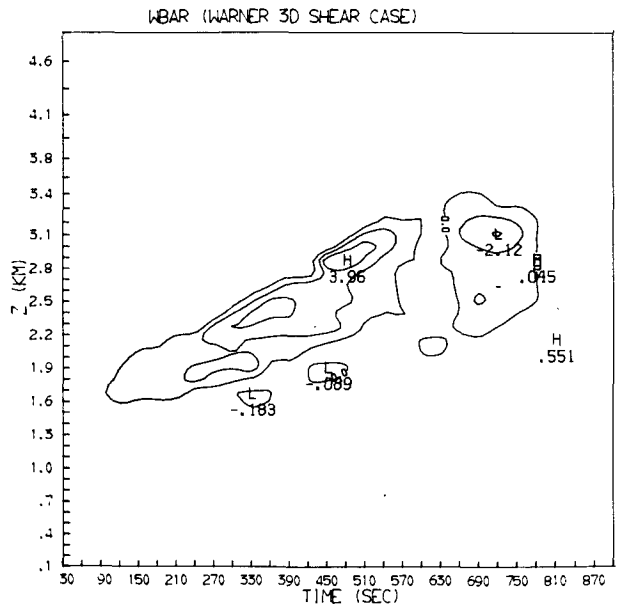

FIG. 19. $\bar{w}$ predicted by 3D experiment assuming a mean sheared wind profile. Labels are m s^{-1}.

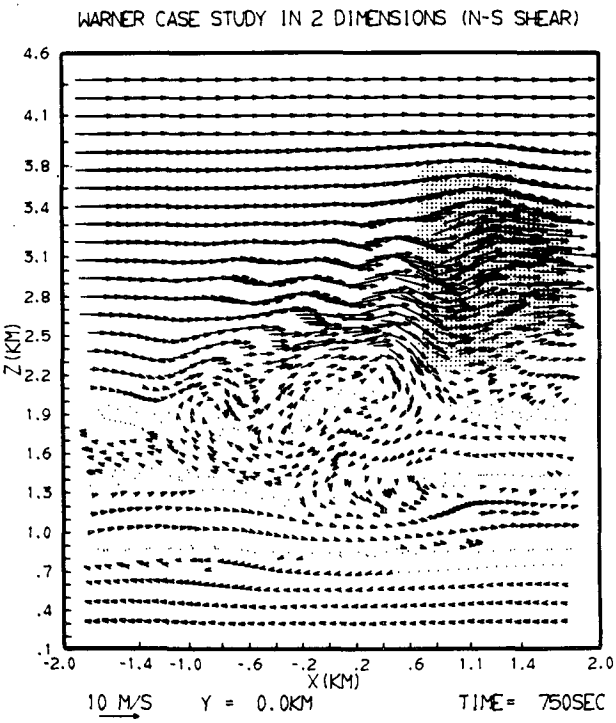

FIG. 20. Wind field and cloud water for 2D experiment assuming the mean sheared meridional wind.

7. Results of a two-dimensional cloud simulation in shear flow

Because the results of the three-dimensional cloud simulations described in the preceding sections illustrate the importance of the interaction of a cloud with environmental wind shear to the prediction of bulk cloud properties, the analysis of the response of a two-dimensional model to shear flow may also be of interest. In this case we choose to simulate cloud growth in the north–south plane (the plane of maximum shear) while assuming no variation in any cloud or environmental property in the east–west direction. Since a number of investigators (Asai, 1964; Orville, 1965; Murray, 1970; Takeda, 1965, 1966; Schlesinger, 1973) have made rather thorough investigations of the response of two-dimensional cloud models to shear flow, a detailed description of the two-dimensional (2D) simulation will not be presented here. The most important feature of the 2D simulation is that the cloud is better able to withstand the destructive effects of shear. Fig. 20, for example, illustrates that the 2D cloud exhibited a vigorous circulation including a broad saturated region even after 750 s of simulated time. The simulated 3D cloud in shear flow, illustrated in Fig. 21, on the other hand, had nearly completely dissipated by that time. In addition, the 2D cloud

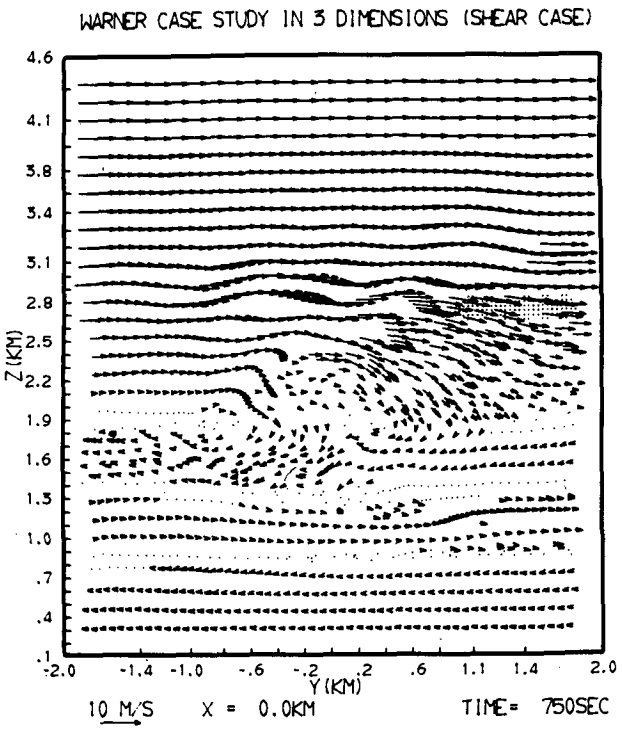

FIG. 21. North–south vertical cross section of wind field and cloud water predicted by the 3D model assuming a mean sheared wind. This corresponds to Fig. 21 which depicts the same field predicted by the 2D model.

grew to a height of 3.71 km, while the 3D cloud in shear flow grew to 3.35 km. The ability of the 2D cloud to better withstand the destructive effects of shear are a consequence of the fact that the 2D cloud experienced only a speed-shear profile. Thus, the dynamically forced entrainment was of weaker magnitude. In addition, the 2D cloud can only experience lateral entrainment in one dimension, while the 3D cloud is exposed to entrainment in two lateral directions. The lower bulk cloud entrainment predicted in the 2D simulation is further illustrated by looking at the predicted profile of $\bar{Q}_c/Q_A$.

Fig. 22 illustrates the predicted time variation of $\bar{Q}_c/Q_A$ for the 2D simulation in shear flow. The first feature of interest is that the profile of predicted $\bar{Q}_c/Q_A$ is structurally a compromise between that predicted by the 3D simulation in shear flow and for a no-motion environment. During the first 5 min of simulated time, the predicted vertical sounding of $\bar{Q}_c/Q_A$ exhibited a considerable lapse with height. Later in the simulation, a tendency for packing of the contours of maximum $\bar{Q}_c/Q_A$ near cloud top is predicted, with magnitudes comparable to those predicted in the 3D no-motion simulation.

In comparison with observation at 1.9 km MSL, the peak predicted values of $\bar{Q}_c/Q_A$ range from 0.31 to 0.35 which is lower than any of the previously discussed predictions. At 2.34 km MSL, the 2D model predicted $\bar{Q}_c/Q_A$ peak magnitudes in the range 0.61–0.63, which is considerably higher than the observed 0.24 value. This is in contrast to the 3D shear-flow prediction of 0.35 to 0.45 and comparable to the 3D no-motion predictions. At 2.77 km MSL, the predicted peak values of $\bar{Q}_c/Q_A$ ranged from 0.53 to 0.61, which is again higher than the observed value of 0.275 and comparable to that predicted in the 3D no-motion simulation.

With the exception of the first observation level, peak values of $\bar{Q}_c/Q_A$ predicted by the 2D model exceeded those observed. The low predicted magnitude of $\bar{Q}_c/Q_A$ at the 1.9 km MSL level is probably indicative of the greater difficulty for the 2D model to develop an organized in-flow at cloud base due to the lack of a second horizontal dimension. At higher levels, on the other hand, the lack of a second horizontal dimension reduces the adverse effects of horizontal entrainment which subsequently leads to the prediction of higher values of $\bar{Q}_c/Q_A$.

8. Summary and conclusions

In preceding sections we have discussed the results of a series of numerical experiments that range from simple, one-dimensional-model calculations [including the discussion in Cotton (1975)] to three-dimensional simulations in a stagnant environment and in shear flow to a two-dimensional simulation in shear flow, all using the same set of case study data. The primary variable chosen for model intercomparison and comparison with observations is $\bar{Q}_c/Q_A$. This variable was selected because it is indicative of the extent that cloud entrainment and mixing have modified the cloud from an isolated, saturated parcel of air. Furthermore $\bar{Q}_c/Q_A$

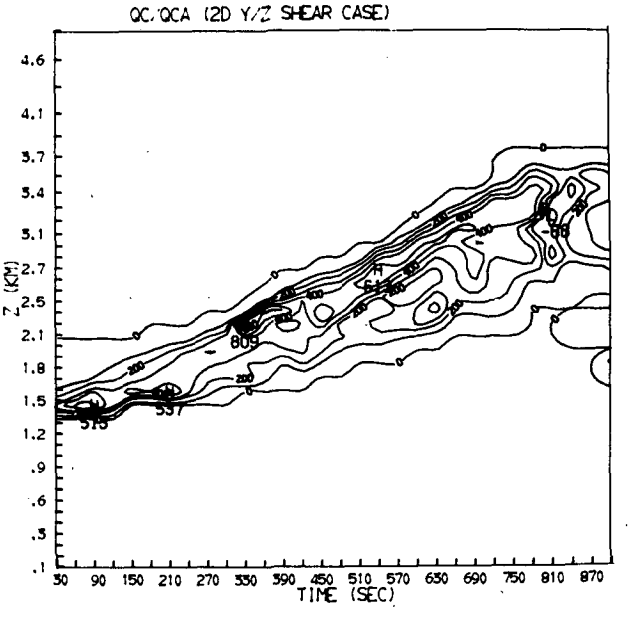

FIG. 22. $\bar{Q}_c/Q_A$ profile for 2D experiment assuming the meridional mean sheared wind of the 3D experiment.

has been found (see Warner, 1970a) to vary rather consistently with height when averaged over a large body of nonprecipitating clouds. In addition, the individual case-study observations discussed above and in Cotton (1975) do not depart significantly from the average profile reported by Warner (1970a). Thus, this variable is a much more reliable indicator of the predictability of a cloud model than is some variable such as cloud-scale-averaged w, which exhibits little temporal and spatial consistency in a cloud.

The results of this study demonstrate that all the cloud simulations in a stagnant environment, including the 1DL, 1DTD and the 3D models, predict profiles of $\bar{Q}_c/Q_A$ which exhibit very high magnitudes near the top of the rising cloud. The predicted magnitudes of $\bar{Q}_c/Q_A$ near the top of the rising cloud exceeded the observed magnitude by as much as a factor of 4. By contrast, the 3D simulation in the observed shear flow predicted profiles of $\bar{Q}_c/Q_A$ which were vertically much more uniform in magnitude at levels above 1.0 km above cloud base. In fact, the magnitude of $\bar{Q}_c/Q_A$ predicted near the top of the rising cloud at upper levels agrees with the observed magnitude to within measurement tolerance.

At the same time the predicted cloud-top height in shear flow was identical to that predicted in the no-motion environment. The apparent insensitivity of predicted cloud-top height to the dynamics associated with shear flow is misleading, however. It could be argued that the strength of the stable layer capping the cumulus layer is so great that all clouds sufficiently vigorous to penetrate into the stable layer will be stopped at roughly the same level by the extreme static stability. This is not consistent with the 1DL and 1DTD model numerical experiments reported by Cotton (1975), however. He found that the 1DL and 1DTD models easily penetrated well above the observed tops and deep into the stable layer when the entrainment coefficient or the eddy-exchange coefficient was lowered in magnitude in those models. Further evidence illustrating the penetrability of the stable layer was given in Section 7. It was found that the 2D cloud grew to a height of 3.71 km, nearly 0.4 km higher than that predicted with either of the 3D simulations.

The fact that the 3D model in the no-motion experiment predicted the observed cloud top height was, in part, by design and, in part, fortuitous. That is, based on our experience with the 1DL and 1DTD models, we selected a moisture perturbation having a horizontal scale and vertical depth that coincided with that used in the 1DTD model. In addition, we employed an eddy exchange coefficient [see Eq. (14)] whose magnitude was calibrated in the 1DTD model by adjusting the coefficient until the observed cloud-top height was predicted. The fact that the actual observed top was predicted with the 3D model to within measurement tolerance was, however, to some degree, fortuitous.

The 3D shear flow numerical experiment was initiated with the same moisture anomaly that was used in the 3D no-motion and the 2D shear flow experiments. Based on our experience with one-dimensional models, one would have anticipated that since the predicted mean Q_c was substantially reduced as a consequence of cloud interactions with shear flow, the predicted cloud-top height should have also lowered. Indeed this was not the case. The fact that the predicted cloud-top height in the 3D shear flow experiment did not exceed that in the no-motion experiment may have been the consequence of a number of factors. First of all, the shear-induced entrainment may have not been sufficient to terminate cloud growth below the height predicted in the 3D no-motion experiment, but may have diluted the cloud buoyancy sufficiently to prevent the cloud from penetrating the stable layer. Second, the increased static stability at the observed cloud-top height was also associated with stronger vertical shear of the horizontal wind at that level. Thus, as the weakly buoyant cloud attempted to penetrate the stable air, the higher vertical wind shear at those levels further inhibited cloud growth.

The shear flow also had a major influence on the prediction of cloud-scale average vertical velocity. This was illustrated by the fact that the predicted maximum cloud-scale average velocity in the shear-flow simulation was only 59% of that predicted in the no-motion simulation. These results illustrate that the interaction of a cloud with shear flow is a particularly nonlinear process in which the entire character and organization of the simulated cloud are dramatically altered.

We thus conclude that the interaction of a cumulus cloud with an environment characterized by vertical shear of the horizontal wind is a major control on the prediction of cloud liquid water contents. This result is somewhat in contradiction to the conclusion of Cotton (1975) who suggested that the source of over-prediction of $\bar{Q}_c/Q_A$ with the 1DTD model was the use of first-order turbulence models. It was thus implied that a higher ordered turbulence model such as those formulated by Sommeria and Deardorff (1977), Lipps (1977) or Manton and Cotton (1977) would alleviate the problem. On the contrary, it appears that, unless one-dimensional models or even two-dimensional models include the parameterization of cloud interaction with shear flow in some realistic manner, they are not likely to successfully predict cloud liquid water contents in general. This is not to say that a three-dimensional model would not be improved by the addition of a higher ordered turbulence parameterization. Indeed, Lipps (1977) has shown that the deformation-eddy-viscosity model consistently produces more cloud water than does a diagnostic, second-order turbulence model. Furthermore, his results, as well as the observations reported by Warner (1970b), Cotton (1975) and Warner (1977), demonstrate a substantial portion of a cumulus cloud's kinetic energy lies on horizontal scales of less than a few hundred meters.

It is simply concluded, however, that the inclusion of a higher ordered turbulence parameterization will not compensate for the inability of one-dimensional and two-dimensional, axisymmetric models to respond to the effects of shear flow.

The simulation of cloud growth in shear flow also exhibited several interesting features, including the formation of a variety of rotating cloud elements. Such vortices are formed as a consequence of the interaction of the cloud momentum field with an environment exhibiting both directional and speed shear of the horizontal wind and which is initially uniform over the horizontal domain of simulation. Because such features may have implications to the formation of tornado-scale vortices, considerably more numerical experimentation should be done to define the factors contributing to single and multiple vortices and their relationships to observed tornado-scale vortex formation. Vortices of this nature, however, have appeared in nearly all the reported 3D cloud simulations in an environment exhibiting directional and speed shear of the horizontal wind including the very simple cumulus cloud simulation discussed above and the deep cumulonimbus cloud simulations reported by Schlesinger (1973), Klemp and Wilhelmson (1978) as well as M. J. Miller (personal communication). It does not appear, therefore, that it will be a simple exercise to isolate cloud-scale vortex features that directly relate to the formation of tornado-scale vortices.

Acknowledgments. The first stages of development of the three-dimensional model were accomplished while one of us (WRC) was an employee of the NOAA Experimental Meteorology Laboratory, Coral Gables, FL. The enthusiastic support of this research by Dr. Joanne Simpson and Dr. William Woodley is greatly appreciated. We would like to acknowledge the helpful suggestions regarding the formulation of the "time-split" compressible calculation provided by Dr. Joseph Klemp of NCAR. Dr. Otis Brown and Mr. Russell Dericksen assisted in programming the model. Ms. Julie Wilson typed the manuscript.

This research was supported under NSF Grant DES 7513310. The numerical experiments were performed at the National Center for Atmospheric Research, which is sponsored by the National Science Foundation.

APPENDIX

List of Variables

Q_c	cloud liquid water mixing ratio
Q_A	moist adiabatic cloud liquid water mixing ratio
P	atmospheric pressure
$U_{i=1,2,3}$	vector air velocity components
$X_{i=1,2,3}$	Cartesian coordinates
$f_{j=1,2,3}$	Coriolis parameter
θ_v	virtual potential temperature
g	acceleration due to gravity
q_v	mixing ratio for water vapor
q_s	saturation water vapor mixing ratio
T	air temperature
T_v	virtual temperature
L_{vl}	latent heat of vaporization
c_p	specific heat at constant pressure
R	specific gas constant for dry air
c_v	specific heat at constant volume
c_{pw}	specific heat for liquid water
K_m	scalar eddy viscosity for momentum
K_H	scalar eddy viscosity for heat
Ri	Richardson number, defined in (17)
θ_e	equivalent potential temperature
D_{ij}	deformation tensor, defined in (18)
t	time
ϵ_{ijk}	permutation symbol
ϵ	ratio of molecular weights of water to dry air
δ_{i3}	Dirac delta function
γ	ratio of specific heat at constant pressure to specific heat at constant volume

REFERENCES

Asai, T., 1964: Cumulus convection in the atmosphere with vertical shear. *J. Meteor. Soc. Japan*, **2**, 245–259.

Asselin, R., 1972: Frequency filter for time integrations. *Mon. Wea. Rev.*, **100**, 487–490.

Cotton, W. R., 1972a: Numerical simulation of precipitation development in supercooled cumuli, 1. *Mon. Wea. Rev.*, **100**, 757–763.

——, 1972b: Numerical simulation of precipitation development in supercooled cumuli, 2. *Mon. Wea. Rev.*, **100**, 764–784.

——, 1975: On parameterization of turbulent transport in cumulus clouds. *J. Atmos. Sci.*, **32**, 548–564.

Deardorff, J. W., 1970: A three-dimensional numerical investigation of the idealized planetary boundary layer. *Geophys. Fluid Dyn.*, **1**, 377–410.

Derickson, R. G., and W. R. Cotton, 1977: On the use of finite Taylor's series approximations to certain exponential and power function employed in cloud models. Atmos. Sci. Pap. No. 268, Colorado State University, NSF Grants ERT-71-01885-A03 and DES75-13310, 19 pp.

Klemp. J. B., and R. B. Wilhelmson, 1978: The simulation of three-dimensional convective storm dynamics. *J. Atmos. Sci.*, **35**, 1070–1096.

Lilly, D. K., 1962: On the numerical simulation of buoyant convection. *Tellus*, **14**, 148–172.

Lipps, F. B., 1977: A study of turbulence parameterization in a cloud model. *J. Atmos. Sci.*, **34**, 1751–1772.

Manton, M. J., and W. R. Cotton, 1977: Formulation of approximate equations for modeling moist deep convection on the mesoscale. Atmos. Sci. Pap. No. 266, Colorado State University, NSF Grant DES 7513310, 62 pp.

Murray, F. W., 1970: Numerical models of a tropical cumulus cloud with bilateral and axial symmetry. *Mon. Wea. Rev.*, **98**, 14–28.

Ogura, Y., 1963: The elevation of a moist convection element in a shallow, conditionally unstable atmosphere, A numerical calculation. *J. Atmos. Sci.*, **20**, 407–424.

Orville, H. D., 1965: A numerical study of the initiation of cumulus cloud over mountain terrain. *J. Atmos. Sci.*, **22**, 684–699.

Robert, A. J., 1966: The integration of a low order spectral form of the primitive meteorological equations. *J. Meteor. Soc. Japan*, **44**, 237–245.

Schlesinger, R. E., 1973: A numerical model of deep moist convection, 1, Comparative experiments for variable ambient moisture and windshear. *J. Atmos. Sci.*, **30**, 835–856.

——, 1975: A three-dimensional numerical model of an isolated deep convective cloud: Preliminary results. *J. Atmos. Sci.*, **32**, 934–957.

Simpson, J., 1971: On cumulus entrainment and one-dimensional models. *J. Atmos. Sci.*, **28**, 449–455.

——, and V. Wiggert, 1971: 1968 Florida cumulus seeding experiment: Numerical model results. *Mon. Wea. Rev.*, **99**, 87–118.

Sommeria, G., and J. W. Deardorff, 1977: Subgrid-scale condensation in models of nonprecipitating clouds. *J. Atmos. Sci.*, **34**, 344–355.

Soong, S. T., and Y. Ogura, 1973: A comparison between axisymmetric and slab-symmetric cumulus cloud models. *J. Atmos. Sci.*, **30**, 879–893.

Takeda, T., 1965: The downdraft in convective shower-cloud under the vertical wind shear and its significance for the maintenance of convective system. *J. Meteor. Soc. Japan*, **43**, 302–309.

Takeda, T., 1966: Effects of prevailing wind with vertical shear on the convective accompanied with heavy rainfall. *J. Meteor. Soc. Japan*, **44**, 129–144.

Warner, J., 1970a: On steady-state one-dimensional models of cumulus convection. *J. Atmos. Sci.*, **27**, 1035–1040.

——, 1970b: The microstructure of cumulus clouds, 3, The nature of the updraft. *J. Atmos. Sci.*, **27**, 682–688.

——, 1977: Time variation of updraft and water content in small cumulus clouds. *J. Atmos. Sci.*, **34**, 1306–1312.

Weinstein, A. I., and L. G. Davis, 1968: A parameterized numerical model of cumulus convection. Rep. II, NSF GA-777, 43, National Science Foundation, Washington, DC, 42 pp.